JACS
JOURNAL OF THE AMERICAN CHEMICAL SOCIETY
pubs.acs.org/JACS

Article

An Ultrasmall Ordered High-Entropy Intermetallic with Multiple Active Sites for the Oxygen Reduction Reaction

Tao Chen,[#] Chunyu Qiu,[#] Xinkai Zhang,[#] Hangchao Wang,[#] Jin Song, Kun Zhang, Tonghuan Yang, Yuxuan Zuo, Yali Yang, Chuan Gao, Wukun Xiao, Zewen Jiang, Yucheng Wang, Yan Xiang, and Dingguo Xia*

Cite This: *J. Am. Chem. Soc.* 2024, 146, 1174−1184

Read Online

ACCESS | Metrics & More | Article Recommendations | Supporting Information

ABSTRACT: Controlling multimetallic ensembles at the atomic level is significantly challenging, particularly for high-entropy alloys with more than five elements. Herein, we report an innovative ultrasmall (~2 nm) PtFeCoNiCuZn high-entropy intermetallic (PFCNCZ-HEI) with a well-ordered structure synthesized by using the space-confined strategy. By exploiting these combined metals, the PFCNCZ-HEI nanoparticles achieve an ultrahigh mass activity of 2.403 A mg_{Pt}^{-1} at 0.90 V vs reversible hydrogen electrode for the oxygen reduction reaction, which is up to 19-fold higher than that of state-of-the-art commercial Pt/C. A proton exchange membrane fuel cell assembled with PFCNCZ-HEI as the cathode (0.03 mg_{Pt} cm^{-2}) exhibits a power density of 1.4 W cm^{-2} and a high mass-normalized rated power of 45 W mg_{Pt}^{-1}. Furthermore, theoretical calculations reveal that the outer electrons of the non-noble-metal atoms on the surface of the PFCNCZ-HEI nanoparticle are modulated to show characteristics of multiple active centers. This work offers a promising catalyst design direction for developing highly ordered HEI nanoparticles for electrocatalysis.

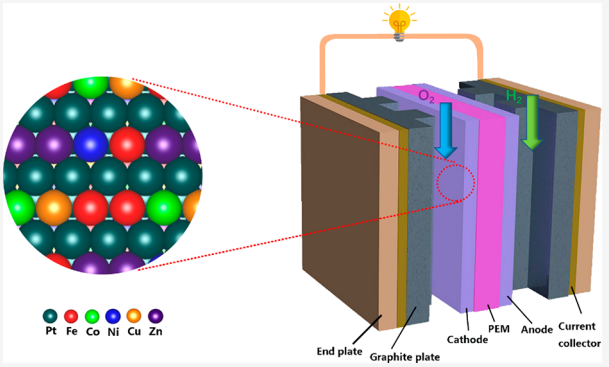

INTRODUCTION

Proton exchange membrane fuel cells (PEMFCs) are considered to be promising sustainable energy systems which can efficiently convert the chemical energy of hydrogen into electrical energy.[1] Nevertheless, the oxygen reduction reaction (ORR), involving multiple electron and proton transfers at the cathode, limits the application of PEMFCs owing to the sluggish kinetics.[2−8] Currently, Pt-based catalysts are still the most essential catalysts for the ORR, demonstrating excellent activity and durability in acidic electrolytes.[9,10] Due to the scarcity of platinum resources and the high cost, the activity of Pt-based catalysts should be urgently improved to reduce the platinum loading in catalysts.[11] Previous studies have revealed that alloying Pt with other transition metals (TMs) is one of the most effective methods for optimizing the surface electronic structure to promote the electrocatalytic performance of Pt-TM catalysts.[12−14] Despite the considerably improved ORR activities, Pt-TMs alloys are commonly prepared as face-centered cubic (fcc)-type solid solution structures, which limits the stability of the TMs under the acidic ORR conditions, thus compromising the advantages of the TMs in Pt-TM alloys.[15,16]

In particular, high-entropy alloys (HEAs), which are composed of five or more elements in similar proportions, have emerged as significant multifunctional catalysts owing to their unique surface electronic structure and physicochemical properties.[17−21] Given their remarkable stability in corrosive media, adjustable composition, and electronic structure, HEAs are highly suitable as efficient electrocatalysts.[22] However, owing to the disordered arrangement of atoms in HEAs, it is difficult to effectively control the surface electronic structure and selectively expose the active sites.

Considering the inherent advantages of well-defined geometric atomic configurations, intermetallic compounds (IMCs) have attracted significant research interest in electrocatalysis applications.[23−26] Compared to metallic alloys with solid solution structures, the well-ordered structures of IMCs can be delicately adjusted to clarify the structure−activity relationship.[27−30] Consequently, by combining the advantages of IMCs and HEAs, high-entropy intermetallics (HEIs) have emerged as promising multifunctional electrocatalysts. However, they have rarely been investigated owing to the difficulties in their synthesis.[31−34] To convert solid solution structures

Received: November 12, 2023
Revised: December 11, 2023
Accepted: December 11, 2023
Published: December 28, 2023

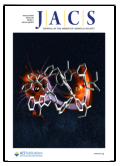

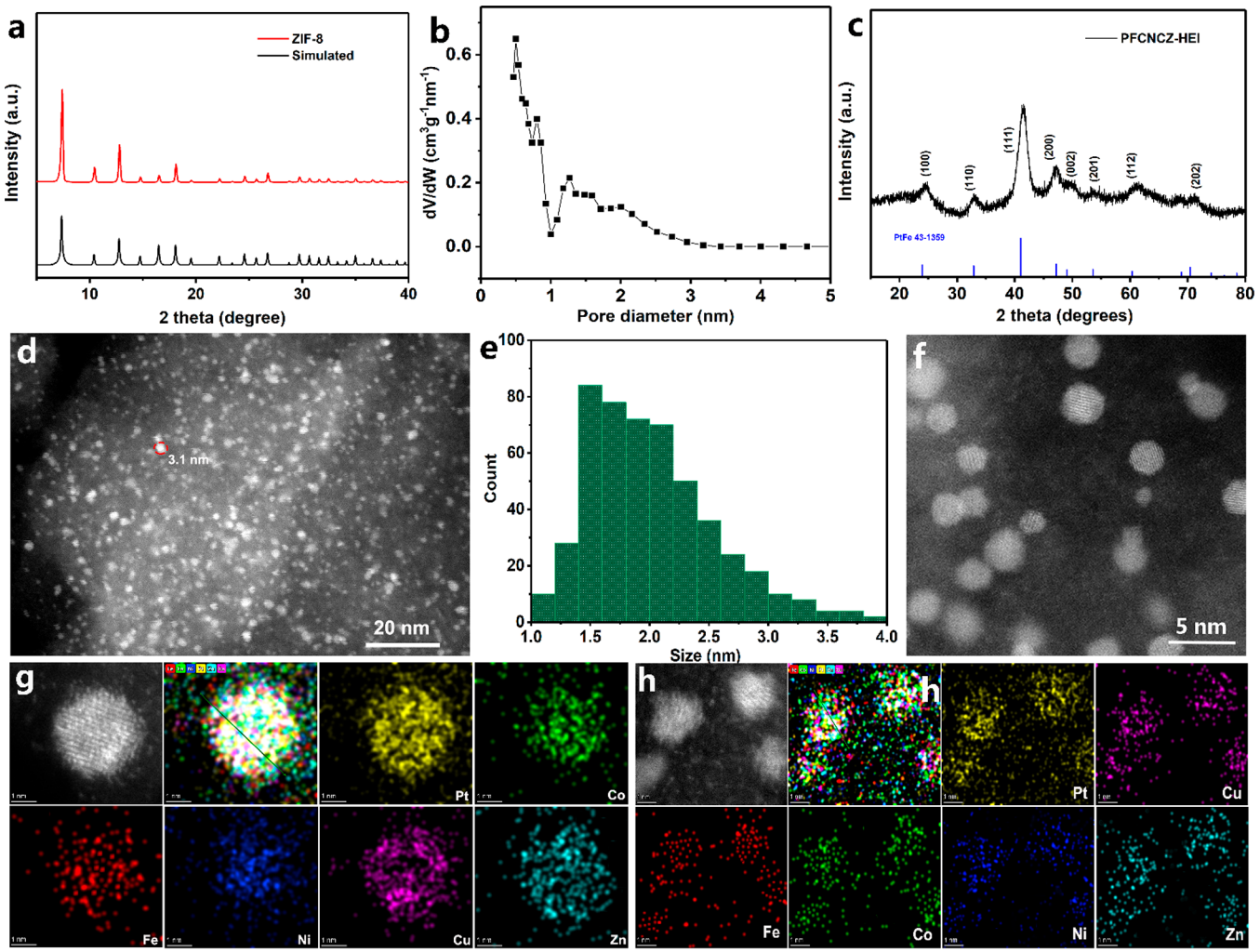

Figure 1. XRD patterns of (a) prepared ZIF-8 and (c) PFCNCZ-HEI, synthesized at 800 °C. (b) Pore size distribution of Zn-DPCN. (d) TEM image of PFCNCZ-HEI. (e) Particle size distribution histogram of PFCNCZ-HEI for (f) local TEM image of PFCNCZ-HEI. STEM-EDS mapping of (g) a single PFCNCZ-HEI nanoparticle and (h) multiple particles.

into IMCs, high-temperature annealing is often required to promote the metal atom arrangement and d-d orbital interaction, leading to large particle sizes (up to 10 nm) and undesirable size distributions.[35,36] Previous experiments and theoretical calculations have demonstrated that, when the nanoparticle size is in the range of 2−3 nm, the mass activity and specific activity can reach the highest values.[37] Therefore, size control of the HEIs is crucial.

To address this challenge, we report the first synthesis of an innovative ultrasmall PtFeCoNiCuZn-HEI (denoted as PFCNCZ-HEI) containing six components with a well-ordered structure via the space-confined strategy. Metal−organic framework (MOF)-derived porous carbon nitride is used as a support to limit nanoparticle growth during intermetallic formation. The as-synthesized PFCNCZ-HEI nanoparticles are among the smallest reported HEIs, with a particle size of approximately 2 nm. Furthermore, they deliver an ultrahigh mass activity of 2.403 A mg_{Pt}^{-1} at 0.90 V vs reversible hydrogen electrode (RHE) for the ORR, which is up to 19-fold higher than that of commercial Pt/C. The PEMFC assembled with PFCNCZ-HEI as cathode (0.03 mg_{Pt} cm^{-2}) achieves a power density of 1.4 W cm^{-2} and a high mass-normalized rated power of 45 W mg_{Pt}^{-1}. The results of density functional theory (DFT) calculations reveal that not only is the Pt site highly active but also non-noble-metal sites are stimulated to be highly active, which significantly improves the ORR performance. The outstanding performance of PFCNCZ-HEI for the ORR provides a potential application to achieve the strategic goal of commercial catalysts for fuel cells.

RESULTS AND DISCUSSION

Structural Characterization. For the synthesis of PFCNCZ-HEI, Zn-based ZIF-8, prepared by the solution heat route, was first pyrolyzed to obtain dodecahedral porous carbon nitride (Zn-DPCN) which contains a certain amount of Zn (Figure S1).[38] It is determined that the Zn element content in the Zn-DPCN carrier is 4.32 wt% by inductively coupled plasma−atomic emission spectroscopy (ICP-AES), as shown in Table S1. Subsequently, the metal salts of Pt, Fe, Co, Ni, and Cu were dispersed and adsorbed into the porous carbon nitride by the immersion method, and a six-element HEI was formed via high-temperature treatment using hydrogen as a reducing gas. During the thermal annealing and electrochemical reaction processes, the pore interaction of this porous carbon nitride support not only hinders nanoparticles aggregation but also effectively inhibits nanoparticle separation.

https://doi.org/10.1021/jacs.3c12649
J. Am. Chem. Soc. 2024, 146, 1174−1184

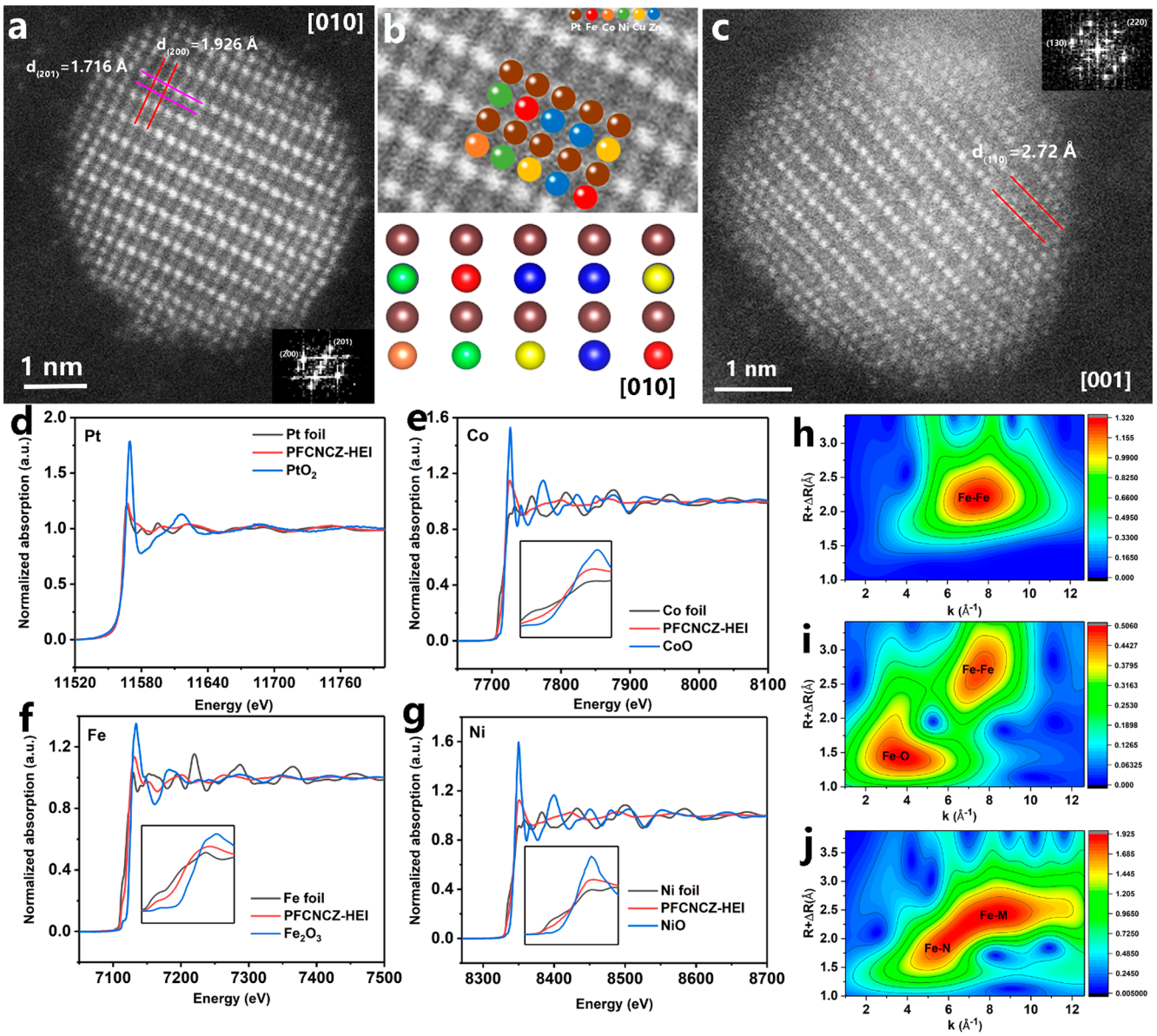

Figure 2. (a, c) HAADF-STEM images of an individual PFCNCZ-HEI nanoparticle. (b) Corresponding local structure image. L_3-edge XANES spectra of Pt (d) and K-edge XANES spectra of (e) Co, (f) Fe, and (g) Ni in the PFCNCZ-HEI nanoparticles. WT-EXAFS plots of (h) Fe foil, (i) Fe_2O_3, and (j) PFCNCZ-HEI for Fe.

The powder X-ray diffraction (XRD) pattern of the prepared Zn-based ZIF-8 corresponds well with that of the simulated ZIF-8, as shown in Figure 1a. Scanning electron microscopy (SEM) images indicate that the structure is a polyhedron with evenly distributed particles (Figure S2). Additionally, Zn-DPCN generated by pyrolysis of the prepared ZIF-8 still maintains the corresponding morphology and size (Figure S3). The N_2 adsorption and desorption isotherms for Zn-DPCN exhibit I/IV-type isotherm characteristic corresponding to micro-/mesoporous materials (Figure S4).[39] Moreover, the overall pore size is less than 3 nm, as shown in Figure 1b. The surface area calculated by the Brunauer−Emmett−Teller (BET) method is up to 1462 $m^2\ g^{-1}$.

Figure 1c presents the XRD pattern of PFCNCZ-HEI, which used Zn-DPCN as the porous support and was synthesized at 800 °C. All the peaks observed for the PFCNCZ-HEI nanoparticles are indexed to a face-centered tetragonal (fct) ordered intermetallic structure with space group *P4/mmm* (JCPDS PDF #43-1359). The fractional elemental composition of Pt/Cu/Co/Ni/Fe/Zn is determined to be 1:0.21:0.16:0.17:0.34:1.67 with a loading of 4.1 wt% Pt in PFCNCZ-HEI by ICP-AES. Sufficient signal intensity and resolution are provided by the synchrotron XRD to identify diffraction peaks of the sample, as shown in Figure S5. All the peaks observed for the PFCNCZ-HEI nanoparticles are indexed to fct ordered intermetallic structure with space group *P4/mmm*. No impurities can be found. When the reduction temperature rises to 900 °C or the loading increases, the corresponding diffraction peaks become stronger (Figures S6 and S7). Transmission electron microscopy (TEM) images reveal that the PFCNCZ-HEI nanoparticles are uniformly dispersed on the support (Figure 1d,f). The particle size of the PFCNCZ-HEI nanoparticles is less than 4 nm, and the average size is approximately 2 nm. Notably, the particle size distribution is consistent with the pore size of the Zn-DPCN support, as shown in Figure 1e. For comparison, Zn-DPCN was replaced

https://doi.org/10.1021/jacs.3c12649
J. Am. Chem. Soc. 2024, 146, 1174−1184

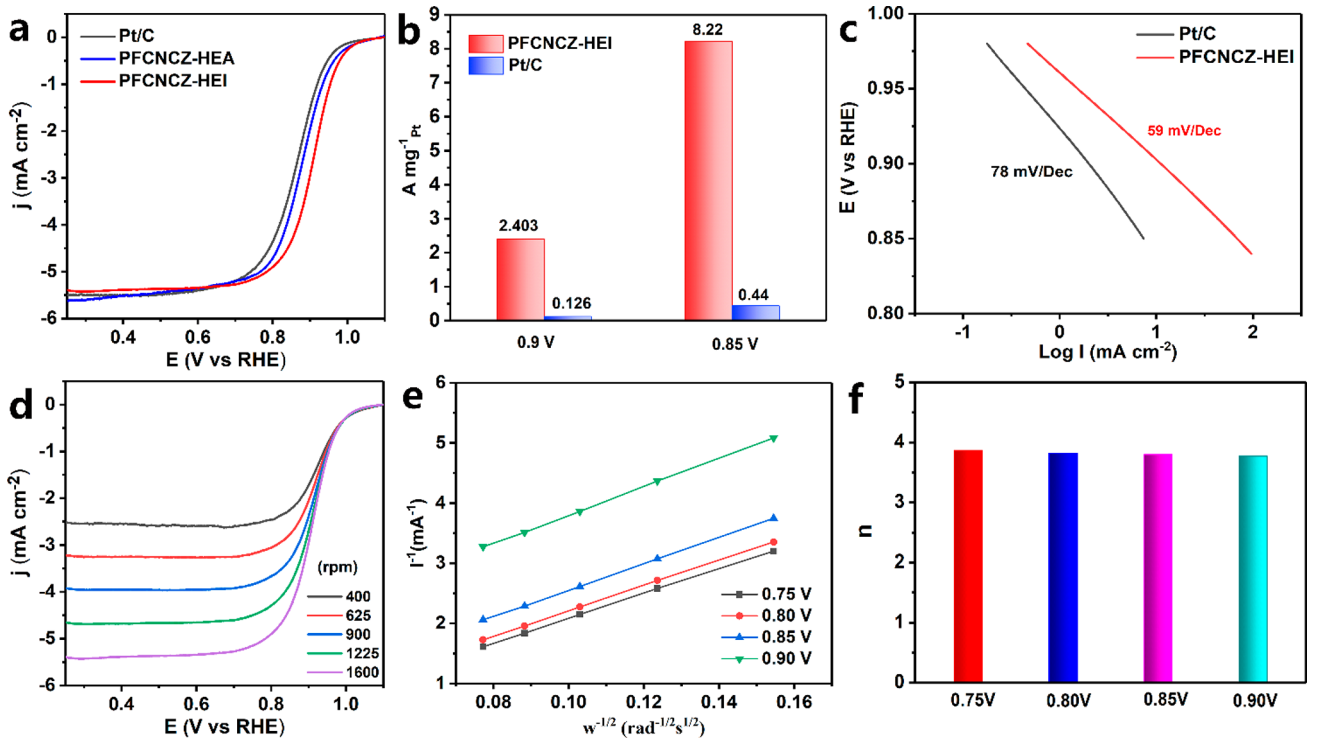

Figure 3. (a) ORR polarization curves of the PFCNCZ-HEI, PFCNCZ-HEA, and commercial 20 wt% Pt/C catalysts. (b) Mass activities at 0.9 V vs RHE and (c) Tafel plots of PFCNCZ-HEI and Pt/C. (d) Polarization curves of PFCNCZ-HEI at different rotation rates and (e) their Koutecky–Levich plots. (f) Charge transfer number of PFCNCZ-HEI.

with XC-72 to prepare the corresponding HEI catalyst (PFCNCZ-XC72) under identical conditions. The crystallinity of PFCNCZ-XC72 is not as high as that of PFCNCZ-HEI (Figure S8). Most importantly, the particle size distribution of PFCNCZ-XC72 is extremely uneven, and the overall particle size is relatively large, with the largest particle being 52 nm (Figure S9). It can be concluded that Zn-DPCN provides spatial confinement to inhibit further particle growth, thus controlling the particle size. Furthermore, distinct (111) crystal planes with a lattice spacing of approximately 0.208 nm are observed, which are highly active crystal planes for the ORR (Figure S10). To evaluate the elemental distribution of the prepared PFCNCZ-HEI nanoparticles, energy-dispersive spectroscopy (EDS) elemental mappings of single nanoparticles are shown in Figure 1g, and those of multiple particles are shown in Figure 1h and Figure S12. It shows that all metals are homogeneously uniformly distributed and well mixed. The atomic ratio of Fe:Co:Ni:Cu:Zn:Pt is measured to be 0.1012:0.0997:0.0912:0.1312:0.0951:0.4816, corresponding to a mixed configuration entropy value of 1.53R, which can be completely defined as a HEI (Figure S13).[39] To further characterize the crystal structure of PFCNCZ-HEI, high-angle annular dark-field scanning transmission electron microscopy (HAADF-STEM) was conducted to reveal the atomic structure of PFCNCZ-HEI. Figure 2a displays a characteristic atomic resolution image of an individual nanoparticle along the [010] zone axis. Because the image intensity is related to the atomic number, the bright spots represent the heavy Pt atoms, while lower contrast spots represent the randomly distributed different light transition metal atoms M in PtM. The fast Fourier transformation (FFT) pattern further defines the [010] zone axis. Lattice spacings of 1.926 and 1.716 Å are measured, corresponding to the (200) and (201) crystal planes, respectively. The periodic arrangement of the atomic column is clearly observed in the locally enlarged image (Figure 2b), which further confirms the order of its structure. Moreover, the (110) crystal plane, with a lattice spacing of 2.72 Å, is observed in Figure 2c, which is the characteristic peak of the fct ordered intermetallic structure.

X-ray absorption near-edge structure (XANES) spectra were collected to investigate the electronic structure of PFCNCZ-HEI. Figure 2d–g and Figure S14a,b exhibit the XANES spectra of the normalized Pt L_3-edge and the Co, Fe, Ni, Cu, and Zn K-edges for PFCNCZ-HEI and related control samples. The "white line" (WL) intensity at the edge of the Pt L_3-edge is significantly lower than that of PtO_2 and slightly higher than that of Pt foil, which indicates that Pt mainly exists in a metallic state. Moreover, the Co, Fe, Ni, Cu, and Zn K-edges indicate an overall approach to their corresponding metal states, but the absorption edges shift slightly toward the high-energy direction. On one hand, the slight shift in the spectrum may be caused by the ligand effect, that is, the transfer of electrons from non-noble-metals to platinum, which shows stronger electronegativity.[38,40] On the other hand, it may be due to charge transfer caused by coupling between the TMs and the N-containing Zn-DPCN support. X-ray photoelectron spectroscopy (XPS) measurements were performed to further evaluate the chemical valence state. The peaks at 71.8, 779.5, 710.0, 853.7, 932.3, and 1022.0 eV are attributed to the corresponding metal states of Pt^0, Co^0, Fe^0, Ni^0, Cu^0, and Zn^0, respectively (Figure S15). Signals corresponding to the respective bivalent states of each metal were also detected. As shown in Figure S16, the N 1s edge of Zn-DPCN before metal loading is divided into graphitic (402.6 eV), pyrrolic (400.9 eV), and pyridinic (398.5 eV) signals. However, in the PFCNCZ-HEI sample loaded with HEI nanoparticles, an

https://doi.org/10.1021/jacs.3c12649
J. Am. Chem. Soc. 2024, 146, 1174–1184

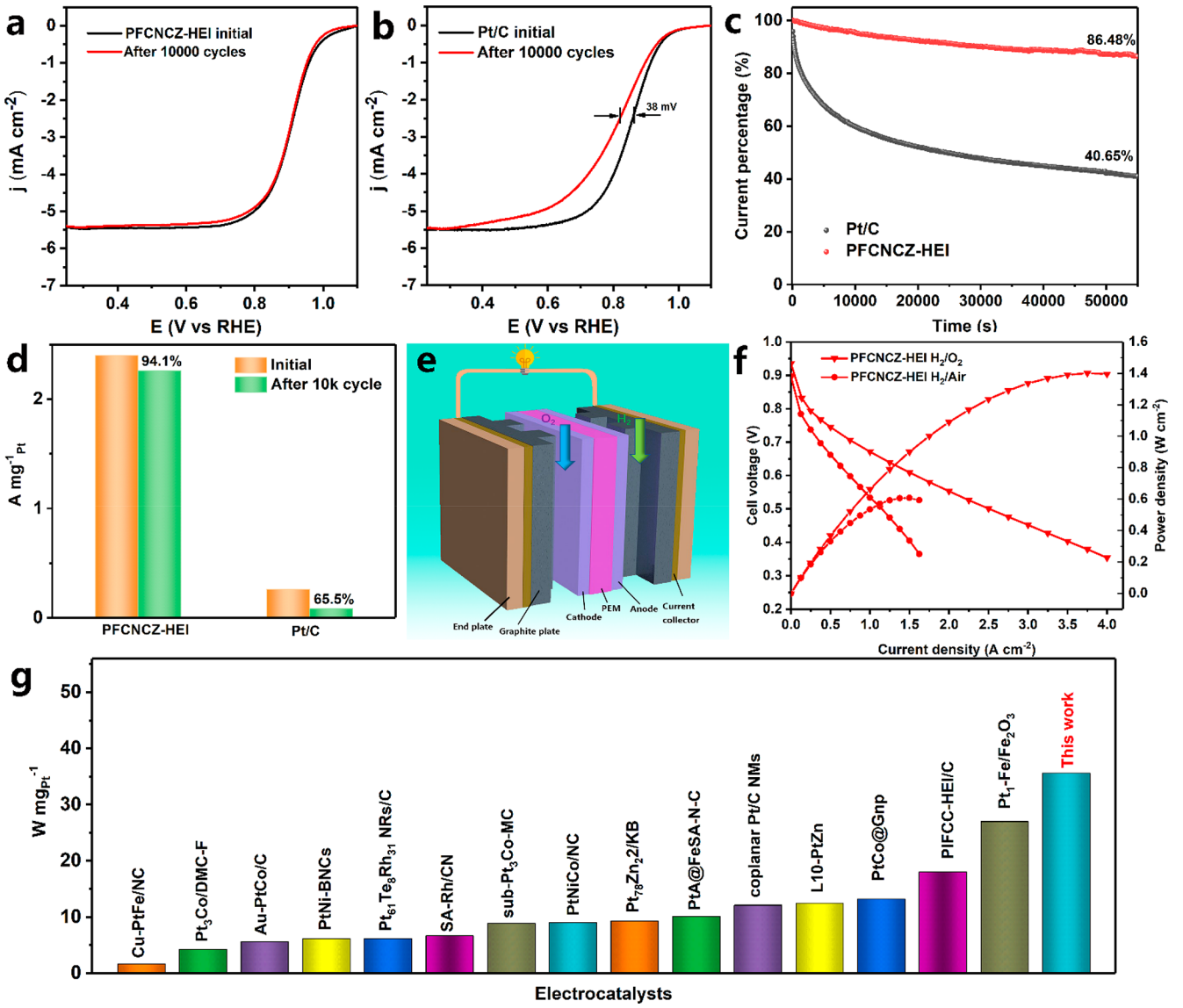

Figure 4. Polarization curves before and after 10 000 cycles for (a) PFCNCZ-HEI and (b) Pt/C. (c) Normalized chronoamperometric curves of the PFCNC-HEI and Pt/C catalysts at a constant potential of 0.7 V. (d) Mass activity before and after ADTs. (e) Schematic view of a typical hydrogen PEMFC and its components. (f) The *I*−*V* polarization curves and power density of a fuel cell made with the PFCNCZ-HEI sample. (g) Comparison of the mass-normalized rated power normalized for the H_2−O_2 fuel cell with PFCNCZ-HEI versus the state-of-the-art catalyst reported in the literature.

additional peak of the metal−nitrogen (M−N) bond is clearly observed at 399.8 eV. As depicted in Figure S17, it can be observed that, in comparison to Pt/C, PFCNCZ-HEI demonstrates a shift of Pt toward higher energy, indicating charge transfer between the support and the metal. The strong bond cooperation between the HEI nanoparticles and support leads to an increase in metal valence state, which is conducive to inhibiting their migration agglomeration in the high-temperature roasting process.

In order to further characterize the coordination structure of the PFCNCZ-HEI nanoparticles, Fourier transform extended X-ray absorption spectroscopy fine structure (FT-EXAFS) k_2-weighted spectra were collected, as shown in Figure S18. The distance of the Pt−M shell in PFCNCZ-HEI (2.3 Å) is slightly shorter than the thickness of Pt foil (2.5 Å), which is attributed to the smaller atomic radius of the TM coordinated with Pt in PFCNCZ-HEI. Furthermore, all six elements show strong M−M peaks, indicating that they exist in the metallic state. It is worth mentioning that the Zn−N bond signal in PECNCZ-HEI is stronger than that of the Zn−M bond peak. When Zn-DPCN is used as the support, part of the Zn exists in the form of Zn-NC, and the other part forms HEIs with other metals.[41,42] The coordination between the support and PFCNCZ-HEI nanoparticles is further determined by wavelet transform (WT) analysis of EXAFS. As shown in Figure 2j, PFCNCZ-HEI exhibits a significant Fe−N signal at approximately 4.3 $Å^{-1}$,[42,43] which is different from the signals for Fe foil (Figure 2h) and Fe_2O_3 (Figure 2i). Additionally, M−N bond signals of PFCNCZ-HEI for Pt, Co, Ni, Cu, and Zn elements are observed (Figures S19−S23), which is consistent with previous reports.[43−45] Combined with the XPS results, the existence of an M−N bond is conducive to anchoring HEI nanoparticles. Local structural information was obtained by fitting the FT-EXAFS spectrum using Artemis software, mainly focusing on fitting the first coordination shell peak of PFCNCZ-HEI owing to the signal-to-noise ratio of the

https://doi.org/10.1021/jacs.3c12649
J. Am. Chem. Soc. 2024, 146, 1174−1184

absorption spectrum for our ultrasmall particles. The fitting quality is shown in Figure S24, and the fitting structural parameters are shown in Table S2. The fitting results indicate that the average coordination number (CN) of the first shell of Pt is 8, with Pt−Pt coordination number of 3.2 and Pt−M (M = non-precious metal) coordination number of 4.8, indicating the successful formation of a fct ordered intermetallic structure in PFCNCZ-HEI.[46]

Electrocatalytic ORR Performance of the Catalysts. The electrocatalytic ORR activity of PFCNCZ-HEI was evaluated using a three-electrode system in acidic 0.1 M $HClO_4$ electrolyte. Additionally, reference samples (including commercial 20 wt% Pt/C and a PFCNCZ high-entropy solid solution alloy denoted PFCNCZ-HEA) and samples synthesized with different loadings, temperatures, and supports were tested and compared under the same conditions. PFCNCZ-HEI shows a higher $E_{1/2}$ (up to 0.906 V) than commercial Pt/C (0.862 V) and PFCNCZ-HEA (0.878 V), as shown in Figure 3a and Figure S25 (error bars displayed), demonstrating that the ordered structure is more conducive to the selective exposure of active sites and the regulation of surface electronic structure. However, after varying the synthesis temperature, increasing the loading, or changing the support to XC72 (denoted as PFCNCZ-XC72), $E_{1/2}$ decreases slightly (Figures S26−S28). Furthermore, the $E_{1/2}$ values for the PtCo, PtNi, PtFe, PtZn, and PtCu binary IMCs are 0.881, 0.874, 0.889, 0.82, and 0.85 V, respectively (Figure S29). This highlights that the cocktail effect resulting from high-entropy alloying leads to unexpectedly enhanced performance compared to that of binary IMCs. Meanwhile, according to the cyclic voltammetry (CV) curves in Figure S30, the electrochemically active surface areas (ECSAs) are calculated to be 69.2 and 68.3 $m^2\ g_{Pt}^{-1}$ for the PFCNCZ-HEI and commercial Pt/C catalysts, respectively. Figure 3b shows that PFCNCZ-HEI delivers a Pt mass-normalized current density of 2.403 A mg_{Pt}^{-1} at 0.90 V vs RHE, which is up to 19-fold higher than that of the commercial Pt/C catalyst (0.126 A mg_{Pt}^{-1}). When the current density is normalized based on all the metal elements, a high total mass activity of 1.64 A $mg^{-1}_{Pt+Co+Fe+Ni+Cu+Zn}$ (13-fold higher than that of Pt/C) is delivered. At 0.85 V vs RHE, the mass activity reaches 8.22 A mg_{Pt}^{-1}, which is 18.7-fold higher than that of Pt/C, superior to the ORR catalysts reported in most literature studies (Table S3). Furthermore, PFCNCZ-HEI exhibits a high ECSA-normalized specific activity of 3.471 mA cm^{-2}, with an excellent improvement factor of 18.9 compared to Pt/C (Figure S31). The Tafel slope (Figure 3c) for PFCNCZ-HEI is only 59 mV dec^{-1}, which is lower than that of Pt/C (78 mV dec^{-1}), indicating that PFCNCZ-HEI shows more outstanding ORR kinetics. The Koutecky−Levich plots in Figure 3e derived from the rotating disk electrode data (Figure 3d) exhibit a good, basically parallel, linear relationship. The number of electrons transferred (n) for PFCNCZ-HEI is calculated to be approximately 4.0, indicating an efficient four-electron mechanism (Figure 3f).

Accelerated durability tests (ADTs) were perfomed to evaluate the electrocatalytic long-term durability of the as-prepared catalysts from 0.6 to 1.1 V in a 0.1 M $HClO_4$ solution. After 10 000 cycles of ADTs, PFCNCZ-HEI exhibits negligible degradation with only 1 mV $E_{1/2}$ attenuation (Figure 4a). The commercial Pt/C displays a 38 mV negative shift of its $E_{1/2}$ after 10 000 cycles of ADTs (Figure 4b). The mass activity losses of PFCNCZ-HEI and Pt/C at 0.9 V vs RHE before and after the ADTs are shown in Figure 4d. PFCNCZ-HEI maintains 94.1% of the initial mass activity after 10 000 cycles, which is considerably higher than observed for commercial Pt/C (only 65.5% of its initial mass activity). Furthermore, the stability is further evaluated by chronoamperometric measurements at 0.7 V. As shown in Figure 4c, the PFCNCZ-HEI catalyst delivers a retention rate of 86.48% after 55 000 s of continuous oxygen reduction, which is considerably higher than that found for Pt/C (only 40.65%). The morphology and composition of PFCNCZ-HEI are further evaluated after a durability test. Figure S33 shows that no obvious agglomeration is observed after 10 000 cycles. In addition, the elements are still uniformly distributed in the nanoparticles (Figure S34). Furthermore, both STEM-EDS mapping (Figure S35) and line scanning (Figure S36) results indicate the absence of significant element segregation after cycling. These results all confirm the high catalytic stability of PFCNCZ-HEI. The extremely high durability of PFCNCZ-HEI may be attributed to the following factors. First, the high-entropy intermetallic structure of PFCNCZ-HEI possesses a high mixed-configuration entropy value of 1.53R and excellent chemical/structural stability. Second, the abundant mesopores of the Zn-DPCN support provide effective protection for PFCNCZ-HEI nanoparticles by confining them in a well-defined mesoporous structure, which effectively inhibits the separation and agglomeration of catalyst particles. Simultaneously, the Zn-DPCN support anchors the nanoparticles through the interaction between N atoms and nanoparticles, thereby significantly inhibiting nanoparticles' migration.

To further verify its remarkable ORR activity, the PFCNCZ-HEI catalyst was used as the cathode in the fabrication of a membrane electrode assembly (MEA), and its actual H_2-O_2 fuel cell performance was tested in PEMFCs. The composition of the membrane electrode is shown in Figure 4e. PFCNCZ-HEI or commercial 20 wt% Pt/C was used as the cathode, and 20 wt% Pt/C was used as the anode. Figure 4f shows the $I-V$ polarization and current−power characteristics tested for PFCNCZ-HEI at H_2-O_2 and H_2−air conditions with a cathodic Pt loading of 0.03 $mg_{Pt}\ cm^{-2}$. As expected, the maximum power densities reach up to 1.4 and 0.6 W cm^{-2} at H_2-O_2 and H_2−air conditions, respectively. In contrast, the maximum power densities of Pt/C are only 1.0 (Figure S37) and 0.41 W cm^{-2} (Figure S38) at H_2-O_2 and H_2−air, respectively. The higher power density of PFCNCZ-HEI indicates a higher ORR activity. Furthermore, the current density at 0.7 V was successfully enhanced, reaching 0.553 W cm^{-2}, much higher than that of Pt/C (0.35 W cm^{-2}). At a voltage of 0.9 V, the mass activity of PFCNCZ-HEI reaches 1.1 A mg_{Pt}^{-1}, surpassing the 2025 U.S. Department of Energy (DOE) target (mass activity >0.44 A mg_{Pt}^{-1} at 0.9 V). In particular, PFCNCZ-HEI delivers a mass-normalized rated power of 45 W mg_{Pt}^{-1} at an O_2 pressure of 2.0 bar, which is considerably higher than that of state-of-the-art ORR catalysts reported in the current literature (Figure 4g and Table S4). In accordance with the ADT protocol established by the DOE, potential cycling in the range of 0.6−0.95 V was conducted to assess the stability of the PEMFC under operational conditions (Figure S39). After 30 000 cycles, PFCNCZ-HEI exhibits a mere 14.3% decay in maximum power density, with negligible degradation observed at 0.8 A cm^{-2}. Finally, a MEA made with PFCNCZ-HEI catalyst was tested constantly at 250 mA cm^{-2}, as shown in Figure S40. After 1000 min of continuous operation, the negligible loss in the working voltage of the

https://doi.org/10.1021/jacs.3c12649
J. Am. Chem. Soc. 2024, 146, 1174−1184

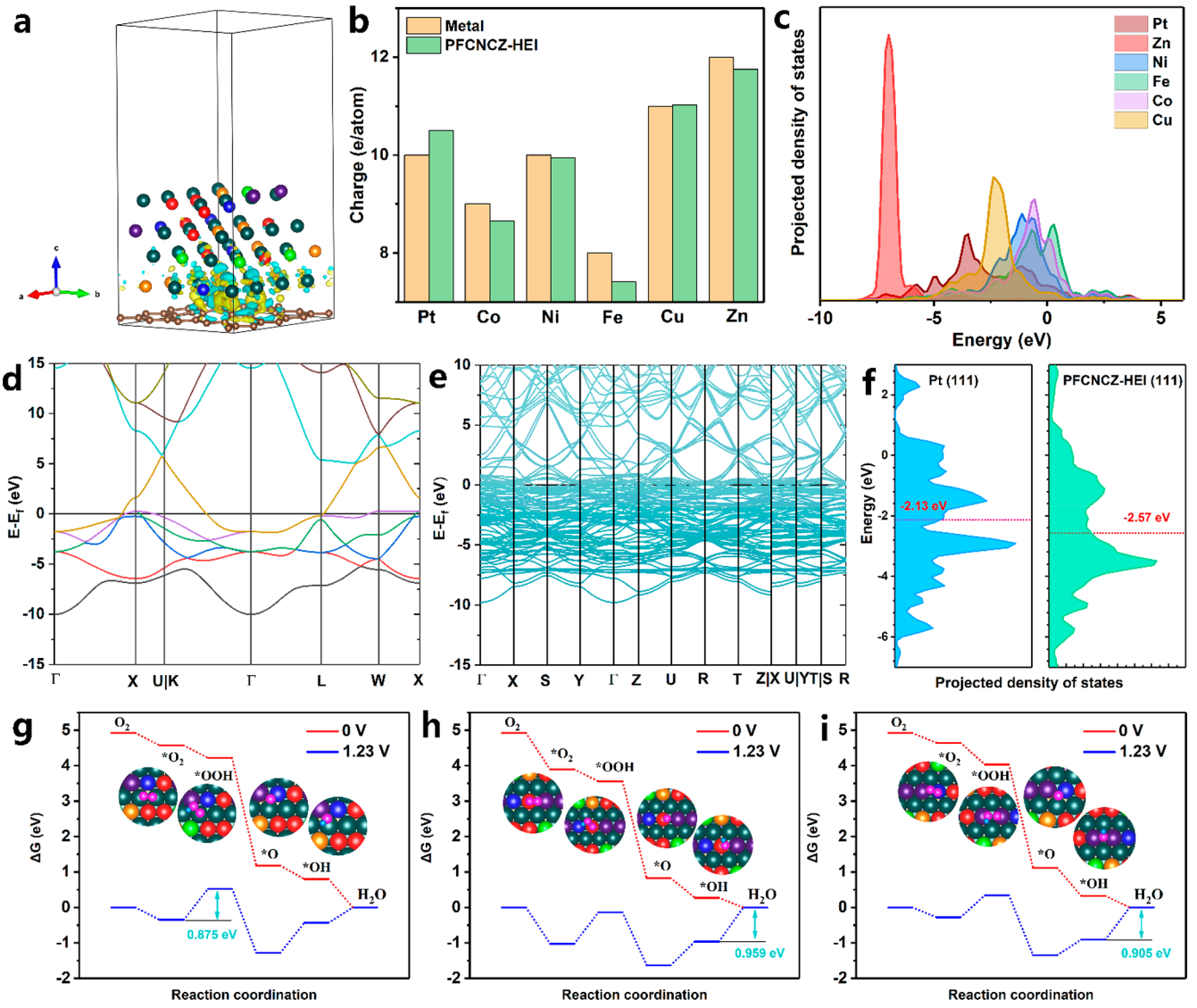

Figure 5. (a) Differential charge density ($\Delta\rho = \rho_{PFCNCZ\text{-}HEI} + \rho_{DPCN} - \rho_{PFCNCZ\text{-}HEI}$) between PFCNZ-HEI and the DPCN support. (b) The number of outermost s and d orbitals' electrons (3d and 4s orbitals for Fe, Co, Ni, Cu, and Zn; 5d and 6s orbitals for Pt) in the surface atoms of PFCNCZ-HEI and the corresponding pure metal. (c) Projected electronic densities of states (PDOSs) of surface Pt-d, Co-d, Ni-d, Cu-d, Zn-d, and Fe-d for PFCNCZ-HEI. Band structure of (d) pure Pt metal and (e) PFCNCZ-HEI. (f) PDOSs of the Pt atom for Pt and PFCNCZ-HEI. Free energies of intermediates of PFCNCZ-HEI for the ORR steps on the (g) Pt28, (h) Fe8, and (i) Zn3 sites.

PEMFC demonstrates the excellent durability and practical application potential of PFCNCZ-HEI.

Density Functional Theory Calculations. DFT calculations were conducted to further elucidate the mechanism of the enhanced ORR performance of PFCNCZ-HEI. In order to simulate the actual environment of PFCNCZ-HEI loaded on DPCN, a layer of porous carbon nitride is constructed under the PFCNCZ-HEI model, as shown in Figures S41 and S42. After a series of model screenings, the surface model from Figure S42a with the lowest surface energy was ultimately chosen as the final computational model. Figure 5a illustrates the charge transfer between the PFCNZ-HEI catalyst and DPCN support, where the isosurfaces in blue and yellow indicate the charge accumulation and depletion, respectively, compared to the system without the DPCN support. Owing to the effect of the DPCN support, the two atomic metal layers at the bottom, in contact with the DPCN, show distinct charge transfer, but the surface atoms are unaffected. This indicates that the DPCN support plays a role in anchoring PFCNCZ-HEI nanoparticles but does not affect the electronic structure of the surface metal atoms. Furthermore, compared to the corresponding pure metals, there is a charge transfer of the outermost s and d orbital electrons between the outer surface metal atoms of PFCNCZ-HEI (Figure 5b). Generally, electrons are transferred from non-noble metals to Pt, caused by the ligand effect, indicating that the electrons on the metal surface are adjusted.[47] The outer electrons of Fe, Zn, Co, and Ni decrease, whereas those of Pt increase, which also leads to a slight change in the valence state of the metals, consistent with the XPS and XANES results. In particular, Zn atoms whose outer electron orbitals ($3d^{10}4s^2$) have been filled appear to have empty orbitals owing to the ligand effect, which is more conducive to bonding with oxygen. The detailed electronic structures of PFCNCZ-HEI are further revealed by the projected partial densities of states (PDOSs) (Figure 5c). Overlaps between the d orbitals of different metals are

https://doi.org/10.1021/jacs.3c12649
J. Am. Chem. Soc. 2024, 146, 1174−1184

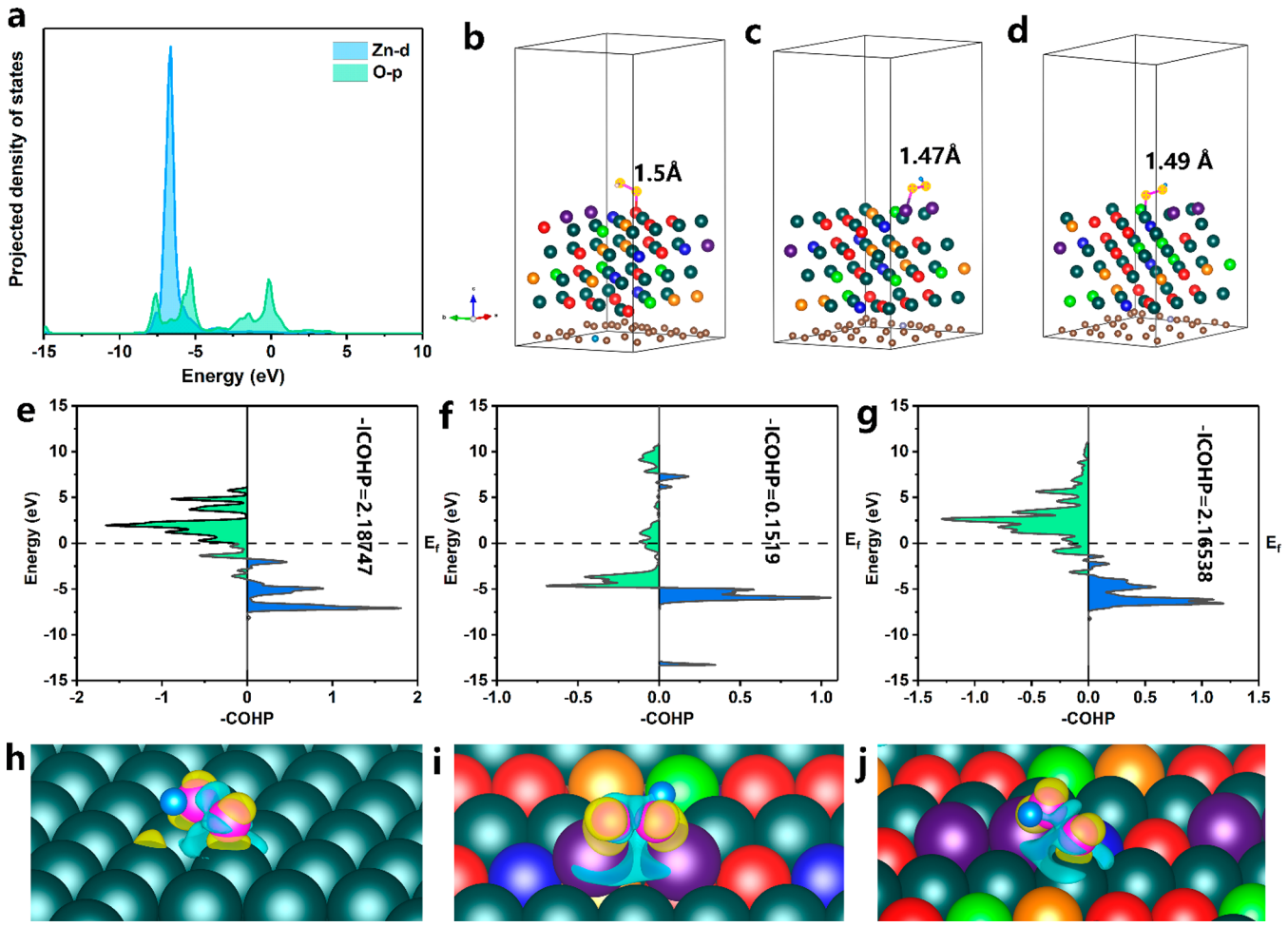

Figure 6. (a) PDOSs of Zn-d and O-p for the Zn3 sites in the $*O_2$ state. O−O bond lengths of *OOH at the (b) Fe8, (c) Zn3, and (d) Pt28 sites. COHP and ICOHP for $*O_2$ adsorption intermediates at (e) Pt (111), (f) the Zn3 site, and (g) the Pt28 site. Differential charge density ($\Delta\rho = \rho_{*OOH} - \rho_{*} - \rho_{OOH}$) of the *OOH adsorbed system at (h) Pt (111), (i) the Zn3 site, and (j) the Pt28 site. The isosurfaces in blue and yellow represent charge accumulation and depletion, respectively.

observed, indicating strong bonds between different metals. Meanwhile, the high electron density indicates a small energy barrier for electron transfer from the PFCNCZ-HEI surface to the adsorbate.[48,49] In contrast, the Pt 5d orbital exhibits a broad band (from −10 to 4.6 eV), which almost overlaps the electron orbitals of all the other elements, indicating that Pt effectively serves as an electron-transfer medium. Furthermore, compared to the energy band structure of Pt (Figure 5d), higher charge density is observed in PFCNCZ-HEI (Figure 5e). As shown in Figure 5f, the d-band center of Pt in PFCNCZ-HEI shifts downward by 0.44 eV compared to that of Pt (111). Moreover, compared to the corresponding pure metals, Co, Cu, Fe, and Ni in PFCNCZ-HEI exhibit smaller band splittings (Figure S43). The d orbital of Zn in PFCNCZ-HEI expands in the high-energy direction, indicating that its surface electrons are optimized, thus improving the degree of overlap with other elements. Furthermore, in comparison to their respective pure metal elements, noticeable broadening of the d-band electronic orbitals for each element is observed in PFCNCZ-HEI, which enhances orbital overlap between elements, facilitating charge transfer between them. This observation also indicates the occurrence of strong bonding between different elements, thereby increasing the structural stability.

In order to further study the ORR mechanism, the Gibbs free energies of the intermediates were calculated. To facilitate identification, the metal sites on the (111) surface of PFCNCZ-HEI are named in turn, as shown in Figure S44. The binding energies of *O and *OH at each metal site are listed in Table S5. According to the research results reported by Rossmeisl et al., non-noble-metal elements with $G_O - G_{OH}$ values between 0.5 and 1.0 eV deliver higher ORR activity.[50] It is concluded that Co2, Fe3, Fe8, Zn2, and Zn3 sites may be highly active sites. Based on this result, several typical sites (Fe8, Zn3, and Pt28 sites) are selected to explore the reaction pathways in more detail. At an equilibrium potential of 1.23 V vs RHE equilibrium potential, the rate-limiting step of Pt (111) is $*O_2$ hydrogenation to form the *OOH intermediate, which shows a ΔG value of 1.006 eV (Figure S45). Similarly, the rate-limiting step of the Pt28 site on the FCNCZ-HEI (111) surface is also the $*O_2$ hydrogenation step, corresponding to a ΔG value of 0.875 eV, which is lower than that of the Pt (111) surface (Figure 5g). Notably, non-noble-metal sites can also undergo efficient four-electron reactions. For the ORR process at the Fe8 (Figure 5h) and Zn3 (Figure 5i) sites, the $*O_2$ adsorption energy is significantly weaker than that of Pt (111), so their rate-limiting steps becomes the last step, which is the transfer of electrons and protons to remove the adsorbed *OH

https://doi.org/10.1021/jacs.3c12649
J. Am. Chem. Soc. 2024, 146, 1174−1184

species. The ΔG values of the rate-limiting steps of Fe8 and Zn3 are only 0.959 and 0.909 eV, respectively, indicating that these non-noble-metal sites have been modulated into highly active sites for the ORR. To the best of our knowledge, Zn is not typically a highly active element for ORR, but it is still promoted to become a highly active site in PFCNZ-HEI. This conclusion further confirms why PFCNCZ-HEI exhibits a total mass activity of 1.64 A $mg^{-1}_{Pt+Co+Fe+Ni+Cu+Zn}$.

The adsorption state of the intermediate is investigated in detail to further elucidate the ORR mechanism. The PDOSs of the d orbitals for the metal sites and p orbitals of O_2 on the PFCNCZ-HEI (111) surface are shown in Figure 6a and Figure S46a,b. The overlap between the Zn-3d and the O-2p orbitals reveals their participation in the Zn−*O_2 bonds. The orbital overlap of the Zn−*O_2 bond is significantly lower than those of the Pt−*O_2 and Fe−*O_2 bonds, demonstrating that the *O_2 adsorption energy at the Zn3 site is weaker than that at the Pt28 and Fe8 sites, which indirectly reduces ΔG for the formation of the *OOH intermediate. The projected crystal orbital Hamilton population (COHP) was used to estimate the interaction between the metal atom and *O_2. Positive (blue area) and negative (green area) values represent the bonding and antibonding contributions, respectively. The integrated COHP value (ICOHP) of the Zn−*O_2 bond was calculated to be 0.1519 (Figure 6f), which is considerably lower than those of the Pt−*O_2 bond (Figure 6g) and the Pt (111)−*O_2 bond (Figure 6e), further demonstrating the relatively weaker bonding of Zn−*O_2. Furthermore, the difficulty in breaking the O−O bond of the *OOH intermediate greatly determines whether the active site undergoes a four-electron or two-electron reaction. The lengths of the O−O bonds at the Fe8 (Figure 6b), Zn3 (Figure 6c), and Pt28 (Figure 6d) sites on PFCNCZ-HEI (111) are almost longer than that on Pt (111) (Figure S47). Additionally, the charge density between the O−O bonds for *OOH at the Zn3 (Figure 6i) and Pt28 (Figure 6j) sites on the PFCNCZ-HEI (111) is significantly lower than that of the Pt (111) surface (Figure 6h). It can be concluded that the O−O bond of the *OOH intermediate at the active site on the PFCNCZ-HEI is more easily broken than that on Pt (111).

CONCLUSION

In summary, we successfully synthesized an innovative ultrasmall PtFeCoNiCuZn HEI with a well-ordered structure using a space-confined strategy. The as-synthesized PFCNCZ-HEI nanoparticles exhibit an average particle size of 2 nm, which is almost the smallest size reported for a high-entropy intermetallic. Compared to the state-of-the-art Pt/C catalyst, the PFCNCZ-HEI catalyst shows distinct advantages, including superior activity and enhanced stability, making it a promising catalyst for the ORR under acidic conditions. The mass and specific activities of the PFCNCZ-HEI catalyst reach 2.403 A mg^{-1}_{Pt} and 3.471 mA cm^{-2} at 0.90 V vs RHE, respectively, which are 19-fold and 18.9-fold higher than those of commercial Pt/C, respectively. Theoretical study results indicate that the modulation of the d-band center of Pt and activation of non-precious-metal sites contribute to the formation of multiple active sites, significantly enhancing the ORR catalytic activity of PFCNCZ-HEI. This study not only presents a viable strategy to fabricate a novel ultrasmall HEI but also provides a sufficiently advanced ORR catalyst for heterogeneous catalytic applications.

ASSOCIATED CONTENT

Supporting Information

The Supporting Information is available free of charge at https://pubs.acs.org/doi/10.1021/jacs.3c12649.

Experimental details, theoretical calculations, and additional characterization data, including Figures S1−S47 and Tables S1−S5 (PDF)

AUTHOR INFORMATION

Corresponding Author

Dingguo Xia − *Beijing Key Laboratory of Theory and Technology for Advanced Batteries Materials, School of Materials Science and Engineering, Peking University, Beijing 100871, P.R. China;* orcid.org/0000-0003-2191-236X; Email: dgxia@pku.edu.cn

Authors

Tao Chen − *Beijing Key Laboratory of Theory and Technology for Advanced Batteries Materials, School of Materials Science and Engineering, Peking University, Beijing 100871, P.R. China;* orcid.org/0000-0002-2334-3431

Chunyu Qiu − *State Key Laboratory of Physical Chemistry of Solid Surfaces, Collaborative Innovation Center of Chemistry for Energy Materials, College of Chemistry and Chemical Engineering, Xiamen University, Xiamen 361005, China*

Xinkai Zhang − *Beijing Key Laboratory of Bio-inspired Energy Materials and Devices, School of Space and Environment, Beihang University, Beijing 100191, China*

Hangchao Wang − *Beijing Key Laboratory of Theory and Technology for Advanced Batteries Materials, School of Materials Science and Engineering, Peking University, Beijing 100871, P.R. China*

Jin Song − *Beijing Key Laboratory of Theory and Technology for Advanced Batteries Materials, School of Materials Science and Engineering, Peking University, Beijing 100871, P.R. China*

Kun Zhang − *Beijing Key Laboratory of Theory and Technology for Advanced Batteries Materials, School of Materials Science and Engineering, Peking University, Beijing 100871, P.R. China*

Tonghuan Yang − *Beijing Key Laboratory of Theory and Technology for Advanced Batteries Materials, School of Materials Science and Engineering, Peking University, Beijing 100871, P.R. China*

Yuxuan Zuo − *Beijing Key Laboratory of Theory and Technology for Advanced Batteries Materials, School of Materials Science and Engineering, Peking University, Beijing 100871, P.R. China*

Yali Yang − *Beijing Key Laboratory of Theory and Technology for Advanced Batteries Materials, School of Materials Science and Engineering, Peking University, Beijing 100871, P.R. China*

Chuan Gao − *Beijing Key Laboratory of Theory and Technology for Advanced Batteries Materials, School of Materials Science and Engineering, Peking University, Beijing 100871, P.R. China*

Wukun Xiao − *Beijing Key Laboratory of Theory and Technology for Advanced Batteries Materials, School of Materials Science and Engineering, Peking University, Beijing 100871, P.R. China*

Zewen Jiang − *Beijing Key Laboratory of Theory and Technology for Advanced Batteries Materials, School of*

Materials Science and Engineering, Peking University, Beijing 100871, P.R. China

Yucheng Wang − *State Key Laboratory of Physical Chemistry of Solid Surfaces, Collaborative Innovation Center of Chemistry for Energy Materials, College of Chemistry and Chemical Engineering, Xiamen University, Xiamen 361005, China;* orcid.org/0000-0002-3356-3403

Yan Xiang − *Beijing Key Laboratory of Bio-inspired Energy Materials and Devices, School of Space and Environment, Beihang University, Beijing 100191, China;* orcid.org/0000-0001-9948-7207

Complete contact information is available at: https://pubs.acs.org/10.1021/jacs.3c12649

Author Contributions

#T. Chen, C.-Y. Qiu, X.-K. Zhang, and H.-C. Wang contributed equilly to this work.

Notes

The authors declare no competing financial interest.

■ ACKNOWLEDGMENTS

We are grateful to Professor Yan Xiang and Master Xinkai Zhang for their contributions to our fuel cells. This work was financially supported by the National Key R&D Program of China under 2022YFB2502100 and the National Natural Science Foundation of China (No. 53130202). All support for this research is gratefully acknowledged.

■ REFERENCES

(1) Debe, M. K. Electrocatalyst approaches and challenges for automotive fuel cells. *Nature* **2012**, *486* (7401), 43−51.

(2) Bu, L.; Zhang, N.; Guo, S.; Zhang, X.; Li, J.; Yao, J.; Wu, T.; Lu, G.; Ma, J.-Y.; Su, D.; Huang, X. Biaxially strained PtPb/Pt core/shellnanoplate boosts oxygenreduction catalysis. *Science* **2016**, *354*, 1410−1414.

(3) Liu, M.; Zhao, Z.; Duan, X.; Huang, Y. Nanoscale Structure Design for High-Performance Pt-Based ORR Catalysts. *Adv. Mater.* **2019**, *31* (6), No. 1802234.

(4) Mo, X.; Deng, Y.; Lai, S. K.; Gao, X.; Yu, H. L.; Low, K. H.; Guo, Z.; Wu, H. L.; Au-Yeung, H. Y.; Tse, E. C. M. Mechanical Interlocking Enhances the Electrocatalytic Oxygen Reduction Activity and Selectivity of Molecular Copper Complexes. *J. Am. Chem. Soc.* **2023**, *145* (11), 6087−6099.

(5) Chang, F.; Xiao, M.; Miao, R.; Liu, Y.; Ren, M.; Jia, Z.; Han, D.; Yuan, Y.; Bai, Z.; Yang, L. Copper-Based Catalysts for Electrochemical Carbon Dioxide Reduction to Multicarbon Products. *Electrochem. Energy Rev.* **2022**, *5* (3), No. 4.

(6) Zhao, J.; Liu, H.; Li, X. Structure, Property, and Performance of Catalyst Layers in Proton Exchange Membrane Fuel Cells. *Electrochem. Energy Rev.* **2023**, *6* (1), No. 13.

(7) Shi, W.; Liu, H.; Li, Z.; Li, C.; Zhou, J.; Yuan, Y.; Jiang, F.; Fu, K.; Yao, Y. High-entropy alloy stabilized and activated Pt clusters for highly efficient electrocatalysis. *SusMat* **2022**, *2* (2), 186−196.

(8) Qiu, H.-J.; Fang, G.; Wen, Y.; Liu, P.; Xie, G.; Liu, X.; Sun, S. Nanoporous high-entropy alloys for highly stable and efficient catalysts. *Journal of Materials Chemistry A* **2019**, *7* (11), 6499−6506.

(9) Hou, J.; Yang, M.; Ke, C.; Wei, G.; Priest, C.; Qiao, Z.; Wu, G.; Zhang, J. Platinum-group-metal catalysts for proton exchange membrane fuel cells: From catalyst design to electrode structure optimization. *EnergyChem.* **2020**, *2* (1), No. 100023.

(10) Xie, M.; Lyu, Z.; Chen, R.; Shen, M.; Cao, Z.; Xia, Y. Pt−Co@Pt Octahedral Nanocrystals: Enhancing Their Activity and Durability toward Oxygen Reduction with an Intermetallic Core and an Ultrathin Shell. *J. Am. Chem. Soc.* **2021**, *143* (22), 8509−8518.

(11) Chen, C.; Kang, Y.; Huo, Z.; Zhu, Z.; Huang, W.; Xin, H. L.; Snyder, J. D.; Li, D.; Herron, J. A.; Mavrikakis, M. J. S.; et al. Highly crystalline multimetallic nanoframes with three-dimensional electrocatalytic surfaces. *Science* **2014**, *343* (6177), 1339−1343.

(12) Kim, C.; Dionigi, F.; Beermann, V.; Wang, X.; Möller, T.; Strasser, P. Alloy Nanocatalysts for the Electrochemical Oxygen Reduction (ORR) and the Direct Electrochemical Carbon Dioxide Reduction Reaction (CO2RR). *Adv. Mater.* **2019**, *31* (31), No. 1805617.

(13) Li, C.; Iqbal, M.; Jiang, B.; Wang, Z.; Kim, J.; Nanjundan, A. K.; Whitten, A. E.; Wood, K.; Yamauchi, Y. Pore-tuning to boost the electrocatalytic activity of polymeric micelle-templated mesoporous Pd nanoparticles. *Chem. Sci.* **2019**, *10* (14), 4054−4061.

(14) Stephens, I. E. L.; Rossmeisl, J.; Chorkendorff, I. Toward sustainable fuel cells. *Science* **2016**, *354*, 1378−1379.

(15) Li, J.; Sharma, S.; Liu, X.; Pan, Y.-T.; Spendelow, J. S.; Chi, M.; Jia, Y.; Zhang, P.; Cullen, D. A.; Xi, Z.; Lin, H.; Yin, Z.; Shen, B.; Muzzio, M.; Yu, C.; Kim, Y. S.; Peterson, A. A.; More, K. L.; Zhu, H.; Sun, S. Hard-Magnet L10-CoPt Nanoparticles Advance Fuel Cell Catalysis. *Joule* **2019**, *3* (1), 124−135.

(16) Feng, G.; Ning, F.; Song, J.; Shang, H.; Zhang, K.; Ding, Z.; Gao, P.; Chu, W.; Xia, D. Sub-2 nm Ultrasmall High-Entropy Alloy Nanoparticles for Extremely Superior Electrocatalytic Hydrogen Evolution. *J. Am. Chem. Soc.* **2021**, *143* (41), 17117−17127.

(17) Fu, X.; Zhang, J.; Zhan, S.; Xia, F.; Wang, C.; Ma, D.; Yue, Q.; Wu, J.; Kang, Y. High-Entropy Alloy Nanosheets for Fine-Tuning Hydrogen Evolution. *ACS Catal.* **2022**, *12* (19), 11955−11959.

(18) Yao, Y.; Huang, Z.; Xie, P.; Lacey, S. D.; Jacob, R. J.; Xie, H.; Chen, F.; Nie, A.; Pu, T.; Rehwoldt, M. J. S.; et al. Carbothermal shock synthesis of high-entropy-alloy nanoparticles. *Science* **2018**, *359* (6383), 1489−1494.

(19) Ding, Q.; Zhang, Y.; Chen, X.; Fu, X.; Chen, D.; Chen, S.; Gu, L.; Wei, F.; Bei, H.; Gao, Y. J. N.; et al. Tuning element distribution, structure and properties by composition in high-entropy alloys. *Nature* **2019**, *574*, 223−227.

(20) Shi, P.; Ren, W.; Zheng, T.; Ren, Z.; Hou, X.; Peng, J.; Hu, P.; Gao, Y.; Zhong, Y.; Liaw, P. K. Enhanced strength−ductility synergy in ultrafine-grained eutectic high-entropy alloys by inheriting microstructural lamellae. *Nat. Commun.* **2019**, *10* (1), No. 489.

(21) McCormick, C. R.; Schaak, R. E. Simultaneous Multication Exchange Pathway to High-Entropy Metal Sulfide Nanoparticles. *J. Am. Chem. Soc.* **2021**, *143* (2), 1017−1023.

(22) Studt, F.; Abild-Pedersen, F.; Bligaard, T.; Sørensen, R. Z.; Christensen, C. H.; Nørskov, J. K. Identification of Non-Precious Metal Alloy Catalysts for Selective Hydrogenation of Acetylene. *Science* **2008**, *320* (5881), 1320−1322.

(23) Zhou, H.; Yang, X.; Li, L.; Liu, X.; Huang, Y.; Pan, X.; Wang, A.; Li, J.; Zhang, T. PdZn Intermetallic Nanostructure with Pd−Zn−Pd Ensembles for Highly Active and Chemoselective Semi-Hydrogenation of Acetylene. *ACS Catal.* **2016**, *6* (2), 1054−1061.

(24) Jia, Z.; Yang, T.; Sun, L.; Zhao, Y.; Li, W.; Luan, J.; Lyu, F.; Zhang, L. C.; Kruzic, J. J.; Kai, J. J.; Huang, J. C.; Lu, J.; Liu, C. T. A Novel Multinary Intermetallic as an Active Electrocatalyst for Hydrogen Evolution. *Adv. Mater.* **2020**, *32* (21), No. 2000385.

(25) Yang, C.-L.; Wang, L.-N.; Yin, P.; Liu, J.; Chen, M.-X.; Yan, Q.-Q.; Wang, Z.-S.; Xu, S.-L.; Chu, S.-Q.; Cui, C.; Ju, H.; Zhu, J.; Lin, Y.; Shui, J.; Liang, H.-W. Sulfur-anchoring synthesis of platinum intermetallic nanoparticle catalysts for fuel cells. *Science* **2021**, *374* (6566), 459−464.

(26) Zeng, Y.; Liang, J.; Li, C.; Qiao, Z.; Li, B.; Hwang, S.; Kariuki, N. N.; Chang, C. W.; Wang, M.; Lyons, M.; Lee, S.; Feng, Z.; Wang, G.; Xie, J.; Cullen, D. A.; Myers, D. J.; Wu, G. Regulating Catalytic Properties and Thermal Stability of Pt and PtCo Intermetallic Fuel-Cell Catalysts via Strong Coupling Effects between Single-Metal Site-Rich Carbon and Pt. *J. Am. Chem. Soc.* **2023**, *145* (32), 17643−17655.

(27) Zhao, S.; Li, Z.; Zhu, C.; Yang, W.; Zhang, Z.; Armstrong, D. E. J.; Grant, P. S.; Ritchie, R. O.; Meyers, M. A. Amorphization in extreme deformation of the CrMnFeCoNi high-entropy alloy. *Sci. Adv.* **2021**, *7* (5), No. eabb3108.

(28) Gamler, J. T. L.; Ashberry, H. M.; Skrabalak, S. E.; Koczkur, K. M. Random Alloyed versus Intermetallic Nanoparticles: A Comparison of Electrocatalytic Performance. *Adv. Mater.* **2018**, *30* (40), No. 1801563.
(29) Yao, Y.; Huang, Z.; Xie, P.; Lacey, S. D.; Jacob, R. J.; Xie, H.; Chen, F.; Nie, A.; Pu, T.; Rehwoldt, M.; Yu, D.; Zachariah, M. R.; Wang, C.; Shahbazian-Yassar, R.; Li, J.; Hu, L. Carbothermal shock synthesis of high-entropy-alloy nanoparticles. *Science* **2018**, *359* (6383), 1489−1494.
(30) Chen, H.; Wang, D.; Yu, Y.; Newton, K. A.; Muller, D. A.; Abruña, H.; DiSalvo, F. J. A Surfactant-Free Strategy for Synthesizing and Processing Intermetallic Platinum-Based Nanoparticle Catalysts. *J. Am. Chem. Soc.* **2012**, *134* (44), 18453−18459.
(31) Dasgupta, A.; He, H.; Gong, R.; Shang, S.-L.; Zimmerer, E. K.; Meyer, R. J.; Liu, Z.-K.; Janik, M. J.; Rioux, R. M. Atomic control of active-site ensembles in ordered alloys to enhance hydrogenation selectivity. *Nat. Chem.* **2022**, *14* (5), 523−529.
(32) Ma, J.; Xing, F.; Nakaya, Y.; Shimizu, K. i.; Furukawa, S. Nickel-Based High-Entropy Intermetallic as a Highly Active and Selective Catalyst for Acetylene Semihydrogenation. *Angew. Chem., Int. Ed.* **2022**, *61* (27), No. e202200889.
(33) Zhu, G.; Jiang, Y.; Yang, H.; Wang, H.; Fang, Y.; Wang, L.; Xie, M.; Qiu, P.; Luo, W. Constructing Structurally Ordered High-Entropy Alloy Nanoparticles on Nitrogen-Rich Mesoporous Carbon Nanosheets for High-Performance Oxygen Reduction. *Adv. Mater.* **2022**, *34* (15), No. 2110128.
(34) Lu, Y.; Huang, K.; Cao, X.; Zhang, L.; Wang, T.; Peng, D.; Zhang, B.; Liu, Z.; Wu, J.; Zhang, Y.; Chen, C.; Huang, Y. Atomically Dispersed Intrinsic Hollow Sites of M-M1-M (M1 = Pt, Ir; M = Fe, Co, Ni, Cu, Pt, Ir) on FeCoNiCuPtIr Nanocrystals Enabling Rapid Water Redox. *Adv. Funct. Mater.* **2022**, *32* (19), No. 2110645.
(35) Zhao, W.; Ye, Y.; Jiang, W.; Li, J.; Tang, H.; Hu, J.; Du, L.; Cui, Z.; Liao, S. Mesoporous carbon confined intermetallic nanoparticles as highly durable electrocatalysts for the oxygen reduction reaction. *J. Mater. Chem. A* **2020**, *8* (31), 15822−15828.
(36) Xie, C.; Niu, Z.; Kim, D.; Li, M.; Yang, P. Surface and Interface Control in Nanoparticle Catalysis. *Chem. Rev.* **2020**, *120* (2), 1184−1249.
(37) Qiao, Z.; Wang, C.; Li, C.; Zeng, Y.; Hwang, S.; Li, B.; Karakalos, S.; Park, J.; Kropf, A. J.; Wegener, E. C.; Gong, Q.; Xu, H.; Wang, G.; Myers, D. J.; Xie, J.; Spendelow, J. S.; Wu, G. Atomically dispersed single iron sites for promoting Pt and Pt3Co fuel cell catalysts: performance and durability improvements. *Energy Environ. Sci.* **2021**, *14* (9), 4948−4960.
(38) Xue, J.; Li, Y.; Hu, J. Nanoporous bimetallic Zn/Fe−N−C for efficient oxygen reduction in acidic and alkaline media. *J. Mater. Chem. A* **2020**, *8* (15), 7145−7157.
(39) Xin, Y.; Li, S.; Qian, Y.; Zhu, W.; Yuan, H.; Jiang, P.; Guo, R.; Wang, L. High-Entropy Alloys as a Platform for Catalysis: Progress, Challenges, and Opportunities. *ACS Catal.* **2020**, *10* (19), 11280−11306.
(40) Tian, X.; Zhao, X.; Su, Y.-Q.; Wang, L.; Wang, H.; Dang, D.; Chi, B.; Liu, H.; Hensen, E. J. M.; Lou, X. W.; Xia, B. Y. Engineering bunched Pt-Ni alloy nanocages for efficient oxygen reduction in practical fuel cells. *Science* **2019**, *366* (6467), 850−856.
(41) Singla, G.; Bhange, S. N.; Mahajan, M.; Kurungot, S. Facile synthesis of CNT interconnected PVP-ZIF-8 derived hierarchically porous Zn/N co-doped carbon frameworks for oxygen reduction. *Nanoscale* **2021**, *13* (12), 6248−6258.
(42) Chen, Y.; Ji, S.; Zhao, S.; Chen, W.; Dong, J.; Cheong, W.-C.; Shen, R.; Wen, X.; Zheng, L.; Rykov, A. I.; et al. Enhanced oxygen reduction with single-atomic-site iron catalysts for a zinc-air battery and hydrogen-air fuel cell. *Nat. Commun.* **2018**, *9* (1), No. 5422.
(43) Guo, W.; Luo, H.; Fang, D.; Jiang, Z.; Chi, J.; Shangguan, W. In situ revealing the reconstruction behavior of monolayer rocksalt CoO nanosheet as water oxidation catalyst. *J. Energy Chem.* **2022**, *70*, 373−381.
(44) Zheng, W.; Chen, F.; Zeng, Q.; Li, Z.; Yang, B.; Lei, L.; Zhang, Q.; He, F.; Wu, X.; Hou, Y. A Universal Principle to Accurately Synthesize Atomically Dispersed Metal−N4 Sites for CO2 Electroreduction. *Nano-Micro Letters* **2020**, *12* (1), No. 108.
(45) Shang, H.; Zhou, X.; Dong, J.; Li, A.; Zhao, X.; Liu, Q.; Lin, Y.; Pei, J.; Li, Z.; Jiang, Z.; et al. Engineering unsymmetrically coordinated Cu-S1N3 single atom sites with enhanced oxygen reduction activity. *Nat. Commun.* **2020**, *11* (1), No. 3049.
(46) Li, J.; Xi, Z.; Pan, Y. T.; Spendelow, J. S.; Duchesne, P. N.; Su, D.; Li, Q.; Yu, C.; Yin, Z.; Shen, B.; Kim, Y. S.; Zhang, P.; Sun, S. Fe Stabilization by Intermetallic L10-FePt and Pt Catalysis Enhancement in L10-FePt/Pt Nanoparticles for Efficient Oxygen Reduction Reaction in Fuel Cells. *J. Am. Chem. Soc.* **2018**, *140* (8), 2926−2932.
(47) Chen, T.; Ning, F.; Qi, J.; Feng, G.; Wang, Y.; Song, J.; Yang, T.; Liu, X.; Chen, L.; Xia, D. PtFeCoNiCu high-entropy solid solution alloy as highly efficient electrocatalyst for the oxygen reduction reaction. *iScience* **2023**, *26* (1), No. 105890.
(48) Tao, L.; Sun, M.; Zhou, Y.; Luo, M.; Lv, F.; Li, M.; Zhang, Q.; Gu, L.; Huang, B.; Guo, S. A General Synthetic Method for High-Entropy Alloy Subnanometer Ribbons. *J. Am. Chem. Soc.* **2022**, *144* (23), 10582−10590.
(49) Zhan, C.; Xu, Y.; Bu, L.; Zhu, H.; Feng, Y.; Yang, T.; Zhang, Y.; Yang, Z.; Huang, B.; Shao, Q.; Huang, X. Subnanometer high-entropy alloy nanowires enable remarkable hydrogen oxidation catalysis. *Nat. Commun.* **2021**, *12* (1), No. 6261.
(50) Busch, M.; Halck, N. B.; Kramm, U. I.; Siahrostami, S.; Krtil, P.; Rossmeisl, J. Beyond the top of the volcano? − A unified approach to electrocatalytic oxygen reduction and oxygen evolution. *Nano Energy* **2016**, *29*, 126−135.

https://doi.org/10.1021/jacs.3c12649
J. Am. Chem. Soc. 2024, 146, 1174−1184